Int. J. of Thermodynamics
ISSN 1301-9724

Vol. 13 (No. 3), pp. 95-103, 2010
www.icatweb.org/ijot

Thermodynamic Optimization of a Monolithic-Type Solid Oxide Fuel Cell*

Adriano Sciacovelli

Department of Energy Engineering, Politecnico di Torino, Turin, Italy
E-mail: adriano.sciacovelli@polito.it

Abstract

In the presented paper possible design modifications in tubular solid oxide fuel cell (SOFC) geometry are investigated in order to increase its performance. The analysis of entropy generation mechanism is very important to optimize the second-law performance of these energy conversion devices. The use of this technique makes it possible to identify the main irreversibilities, understand their causes and propose changes in the system design and operation. The various contributions to the entropy generation are analyzed separately in order to identify which are the main geometrical parameters to be considered as the independent variables in the optimization procedure. The optimization is applied to a CFD model of the fuel cell which accounts for energy equation, fluid dynamics in the channels and in porous media, current transfer, chemical reactions, electrochemistry and raditive heat transfer. The entropy generation is computed as a post-processed quantity with the data obtained for the CFD model. The geometrical parameters of the fuel cell are modified to minimize the overall entropy generation. Boundary conditions to the CFD model are provided with the aid of a reduced thermal model to take in account stack operating condition.

Keywords: *SOFC, entropy generation.*

1. Introduction

Solid oxide fuel cells (SOFCs) are considered promising energy conversion devices thanks to their several potential benefits, including low pollutant emissions, high-energy efficiency, the possibility of using different kinds of fuels and the possibility to build hybrid systems. One of the big advantages of high temperature fuel cells resides in their theoretical efficiency (Larminie and Dicks, 1999). Nevertheless, SOFC technology is still in an embryonic state and different problems must be solved in order to achieve the goal of a highly efficient and reliable energy system. Current SOFC installations are characterized by higher efficiencies than other technologies available for distributed power generation (Verda et al., 2008), however there are margins for increasing the overall efficiency.

One of the causes of efficiency reduction is related to the transport phenomena that take place inside the SOFCs: non-uniformities in physical quantities such as temperature, concentrations, mass flow rates, etc. are the origin of thermodynamics irreversibility, and ultimately induce inhomogeneous distributions in current densities and power production. This cause is investigated in this paper, together with possible improvements that can be achieved through changes in the fuel cell geometry.

A tubular-like SOFC configuration, obtained starting from a mono-block-layer built (MOLB) fuel cell and adding an air injection tube, is here considered. A longitudinal cross section of the geometry is analyzed and the corresponding stack is shown in Figure 1. The fuel cell is composed of a solid electrolyte layer (in yellow) between a porous cathode (in red) and anode (in blue). Above and below this matrix there are two interconnections (in grey). Fuel and air flows in trapezoidal channels, but air is introduced through an injection tube located inside the cathodic channel.

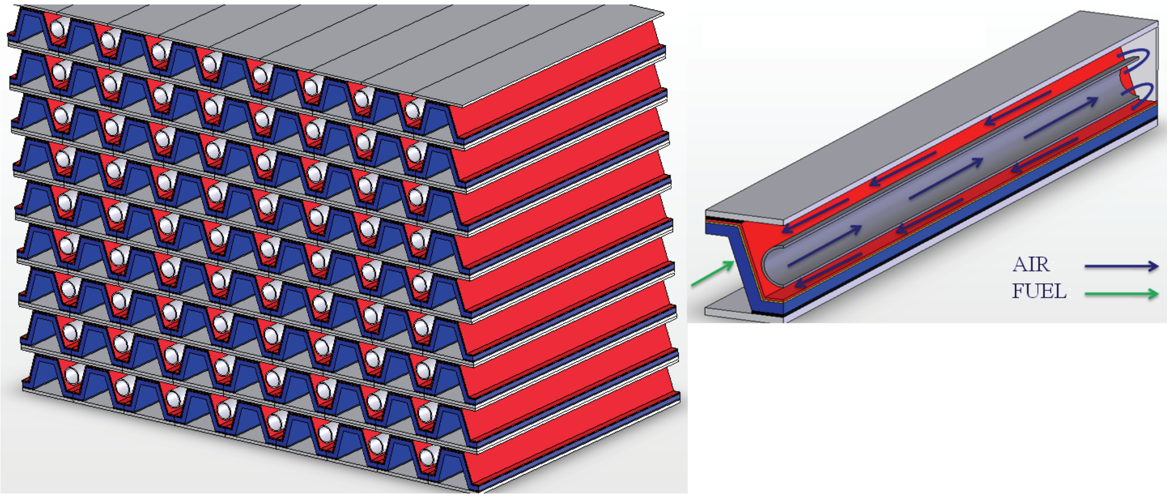

Figure 1. Geometry of the stack and single fuel cell.

*This paper is an updated version of a paper published in the ECOS'09 proceedings. It is printed here with permission of the authors and organizers.

In this way, air flows from the top end of the cell to the bottom end exchanging heat but without variations in chemical composition. Air exiting the tube flows in the trapezoidal air channels from the bottom to the top in counter-current configuration with respect to fuel flow models. Because of the peculiar shape of the ensemble of electrodes+electrolyte (PEN), MOLB are characterized by higher reactants utilization, which allows to obtain higher current density with respect to planar cells (Y. Yang et al., 2008). For a complete overview of the peculiar features of MOLB SOFCs the interested reader may read (J.J. Hwang et al., 2005).

In this paper, second law analysis is used to highlight the major causes of inefficiencies and locate where they occur. This picture helps one to identify possible ways to improve the fuel cell design. The local entropy generation rates are calculated by using a CFD model which accounts for heat and mass transfer as well as chemical and electrochemical reactions. When CFD models are adopted to study SOFCs, the analysis is usually focused on a single isolated fuel cell because of limitations due to the large computational resources required. This approach has been widely adopted in the literature (Pramuanjaroenkij et al., 2007), however it has been observed experimentally that usually the cells in a stack do not operate uniformly (Gubner et al., 2003). In particular SOFCs stacks are characterized by significant non-uniform temperature distribution. Thus isolation conditions are not usually representative of real operating conditions.

In this paper a possible stack configuration based on the MOLB fuel cell with air injection tube is proposed; in particular, the stack is constituted of 81 cells and depicted in Figure 1. CFD approach is feasible for stack analysis only when a very small number of cells is considered (Lee and Hong, 2010), for this reason SOFC stacks are usually analyzed with the aid of reduced models generally focused on a specific aspect of the problem (Ki and Kim, 2010). In this work a reduced thermal model has been adopted to provide proper boundary conditions to the single fuel cell CFD model.

2. Mathematical Model

The single fuel cell illustrated in Figure 1 is analyzed using a Computational Fluid Dynamics (CFD) model, which provides a detailed description of physical phenomena taking place in fuel cells as well as the effect of the geometry on these phenomena. A three-dimensional CFD model accounting for heat and mass transfer as well as chemical and electrochemical reactions is used. The model consists of 7 partial differential equations which are solved in each domain: continuity equation, momentum equation (3 components), energy equation, conservation of species and conservation of charge. The model has been developed using the commercial code Fluent©.

The Navier-Stokes equation is considered for fluid flow in the channels while the Brinkman-extended Darcy equation is used for the porous media. The diffusive flux of species is computed with Stefan–Maxwell equations (Krishna and Wesselingh, 1997). The effects of porous media on diffusion process is taken into account through modified binary diffusivities. The active reaction sites, the three-phase boundaries (TPB), are considered to be located on the surface between electrolyte and electrodes. On these surfaces, the generation/destruction of species is related with the current through Faraday's law. In addition, conversion of electronic current into ionic current and vice-versa is governed by the Butler-Volmer equation.

The following hypotheses are considered: steady state conditions, gas mixtures are considered ideal gas, the fluid flow is laminar and incompressible, porous electrodes are homogeneous and isotropic with uniform morphology proprieties such as porosity, tortuosity and permeability, and thermal equilibrium between solid phase and gas is considered in the porous media.

This model was proposed in (Sciacovelli and Verda, 2008); here radiation heat transfer in the fuel cell is also considered. In the papers available in literature, often this contribution is neglected (see for example Li and Suzuki, 2004). The reason for such an assumption is that, when a single isolated fuel cell is considered (as it is usually considered in the literature), radiation heat transfer is in most cases negligible. An important exception is represented by tubular solid oxide fuel cells, where there is a large radiation heat transfer between the cathode surface and the fresh air injection tube. This effect is not negligible (Ota et al., 2003; Haynes and Wepfer, 2001) and the temperature profiles that are obtained considering it or not are significantly different (Fischer and Seume, 2006).

Modeling of thermal radiation propagation in the general case of participating media requires solution of the radiative transfer equation (RTE), an integro-differential equation which must be solved numerically:

$$\frac{\partial I}{\partial s} = -(a+\sigma_s)I + a\frac{n^2\sigma T^4}{\pi} + \frac{\sigma_s}{4\pi}\int_0^{4\pi} I(\vec{s}_i)\Phi(\vec{s}_i,\vec{s})\,d\Omega_i \qquad (1)$$

where $I(\vec{r},\vec{s})$ is the radiation intensity, which depends on position $\vec{r}$ and direction $\vec{s}$, a the surface absorption coefficient, σ_s the scattering coefficient, n the refractive index and $\Phi(\vec{s},\vec{s}')$ the phase function.

The discrete ordinate (DO) (Chui and G. D. Raithby, 1993) has been used in order to solve the radiative transfer equation. In particular the DO model solves the RTE equation for a finite number of discrete solid angles, each associated with a direction vector $\vec{s}$ fixed, moreover it is applicable for any optical thickness. When solid oxide fuel cells are analyzed, in general one needs to consider emission and reflection of radiation by the walls as well as its extinction and emission by the flowing gases. Air mainly consists of simple non-polar nitrogen and oxygen molecules and, therefore, is non-interacting (transparent) with thermal radiation at the moderate pressures and temperatures found in SOFCs (Modest, 2003). For the fuel channels, however, the analysis is more complicated due to the presence of H_2O. Nevertheless, Damm and Fedorov (2005) showed that for typical SOFCs dimensions the medium can also be treated as transparent. Thus surface-to-surface radiation exchange is the only radiative transfer mode considered in this paper. The solution method of Eq. (1) is identical to that used for the fluid flow and energy equations. The fineness of the angular discretization has been properly chosen to guarantee a grid independent solution.

The radiative heat flux can be computed from the radiation intensity by integration:

$$q_r = \int I(\vec{r},\vec{s})\,\vec{s}\,d\Omega \qquad (2)$$

With regards to the entire stack, it has been modeled using a network approach. The model is based on the approach proposed by Verda and Calì (2007). Further details can be found at (Ciano et. al., 2010). A schematic of a portion of the network is shown in Figure 2. Only the thermal problem is solved. Each cell is represented as composed of seven interconnected elements, divided into longitudinal portions (called branches): cold air flowing in the injection tube (A), hot air flowing outside the tube (B), four elements for the cathode+electrolyte+anode (C-F) and the fuel (G). Nodes are the interconnections between elements. Each node is characterized by a unique temperature.

Energy equation is written for the branches. This equation is written in the general form:

$$\Phi = K \cdot (T_{out} - T_{in}) \qquad (3)$$

where Φ is the heat flux generated in the branch, and K is the conductance associated with the branch. This term may account for conduction, convection or convective fluid flow. Concerning boundary conditions, the inlet temperature of fluids is set and a condition of convective flow is set in the nodes where fluids exit the system. The result is constituted by the four heat fluxes exchanged by each cell and the surrounding cells.

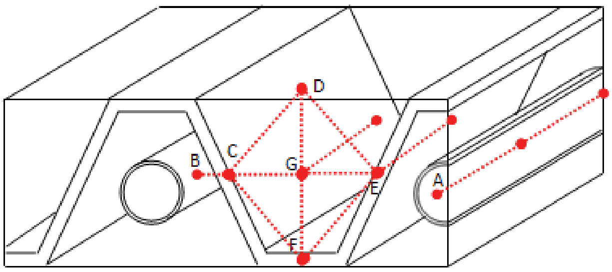

Figure 2. Schematic portion of network thermal stack model.

3. Simulation of different fuel cells within the stack

The model introduced in the previous section couples electrochemical calculation with computational fluid dynamics. The Navier–Stokes equation and transports equations are discretized by using the finite volume method (FVM) to obtain velocity field, temperature and mass fractions in the fuel cell. The local current density is then computed and source term for species and energy equation are determined. This procedure is repeated until convergence is reached. In the equations, the convective terms are modeled by second order upwind scheme while the diffusive terms are modeled by the central difference scheme. The numerical solution procedure adopts the semi-implicit SIMPLE algorithm (Patankar, 1980).

Along the two longitudinal mid-planes of air and fuel channel heat flux is imposed. The value of the heat flux is obtained with the thermal stack model. Therefore the CFD single cell model is one-way coupled with the reduced stack model. Analogous conditions are applied along the planes corresponding to fuel cell interconnections. These boundary conditions take into account the temperature gradients within the stack. These non-uniformities in stack temperature cause a net heat flow from cell to cell, thus adiabatic conditions are not suitable for modeling real operating conditions of a fuel cell in a stack. Moreover in the simulations the air and the fuel are supplied at 973°C, and the faces of the stack exposed to surrounding are assumed to be isolated. Table 1 shows details of the fuel cell geometry. Further dimensions and design parameters of the fuel cell configuration considered can be found in (Sciacovelli and Verda, 2009).

Table 1. Geometrical parameters

Anode	Thickness (mm)	1.4
Cathode	Thickness (mm) Axial length (mm)	0.4 17
Electrolyte	Thickness (mm) Axial length (mm)	0.1 17
Fuel channel	Length (mm) Cross section (mm^2)	100 90
Air channel	Length (mm) Cross section (mm^2)	100 80
Injection tube	Diameter (mm)	10

Two different fuel cells of the stack have been analyzed: the first is located in the middle of the stack where more uniform conditions are present. The second cell is situated at the upper-left corner of the stack, thus two sides of the fuel cell are isolated. As an example, total heat flux entering the right longitudinal mid-plane of the two cells as a function of the cell length are illustrated in Figure 3. The heat flux is obtained with the stack network model. The case of the cell in the center is represented by the blue line, while the red plot refers to the cell in the periphery: the top-left cell exchange a larger heat flux through the surface corresponding to the air-tube mid plane, although the overall heat flux exchanged through the four external surfaces is higher in the case of the cell in the center of the stack, as illustrated in Figure 4. This is due to the fact that the top-left cell presents two isolated surfaces, namely the top plane and the left longitudinal plane; whereas the central cell exchanges heat through all its four surfaces.

The first case considered is the cell situated in the centre of the stack: Figure 5 shows the velocity field inside the injection tube and the cathodic channel. The air flows in the tube from the top of the cell to the bottom. At the closed end of the channel two vortexes take place. This is typical of tubular fuel cell. Air flows back from the bottom end to the top in the cathode channel. It is interesting to observe that in the lower part of the channel the velocities are higher; this is due to a smaller cross-section below the air tube.

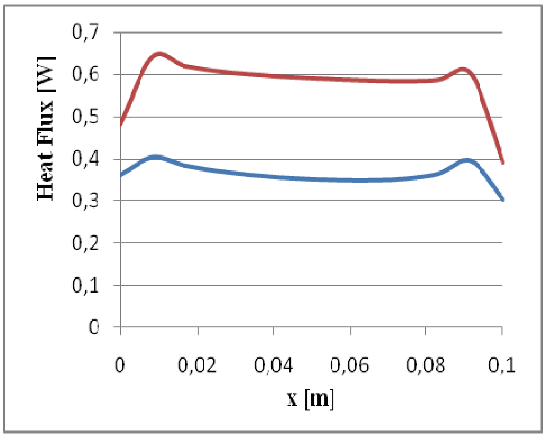

Figure 3. Heat flux entering the right longitudinal plane of the central cell (blue) and the top-left cell (red).

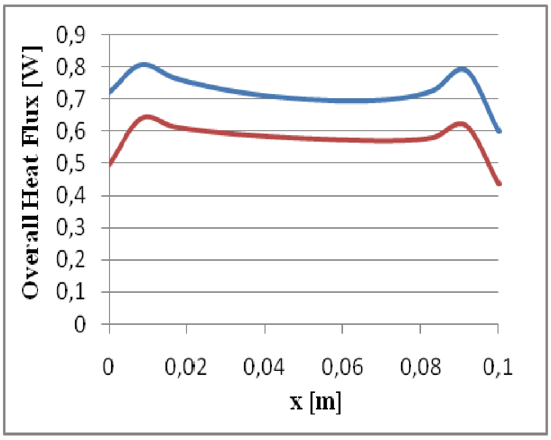

Figure 4. Overall heat flux entering the central cell (blue) and the top-left cell (red).

In the porous electrodes the flow is mainly driven by diffusion phenomena: in the anode the net flow is directed to the fuel channel. This is due to the production of water because of electrochemical reaction. At cathode side, oxygen is consumed, thus the air flows from the channel to the cathode.

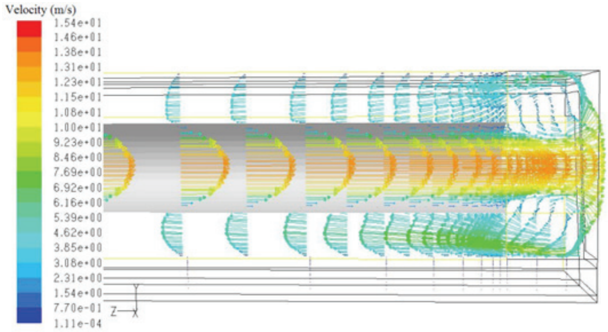

Figure 5. Velocity field inside cathode channel.

Figure 6 shows the hydrogen concentration at anode side along several transversal cross sections. It is clear that hydrogen mass fraction has a strong gradient in streamwise directions, and this profile is characterized by the rate of consumption of hydrogen due to electrochemical reactions. From Figure 5 it is also evident that a concentration gradient takes place also in transversal direction. This is the result of hydrogen diffusion process from bulk flow to the three-phase boundary, in particular this effect is stronger in the lower zone of the anode, where hydrogen mass fraction is smaller.

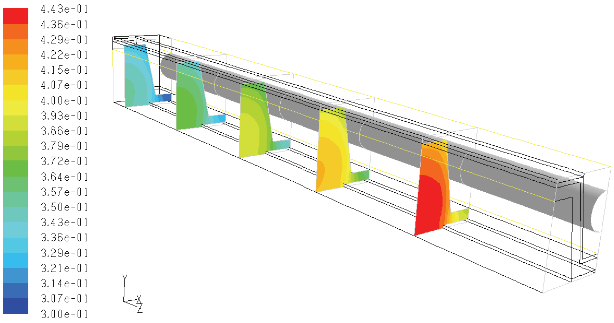

Figure 6. Distribution of hydrogen mass fraction.

In Figure 7, the oxygen mass fraction in the cathode channel is depicted. Since air flows inside the tube first, the higher oxygen concentration is localized in the bottom part of the cell. As in the case of the hydrogen, oxygen mass fraction presents variation both in streamwise direction and in the *x-y* plane. In particular the oxygen cannot reach easily the upper plane of the cathode, this occurs because the porous matrix on cathode side represents an obstacle to the air flow.

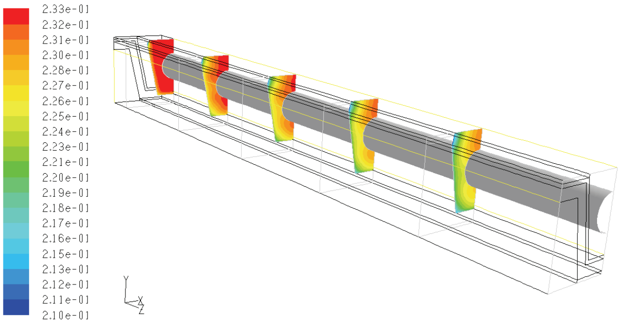

Figure 7. Oxygen mass fraction.

Electrochemical reactions release heat according to the change in entropy of the reaction, charge currents generate Joule heating and activation polarization is translated in heat source (Pramuanjaroenkij et al 2007). Thus, an overall increase in the cell temperature is expected with respect to the inlet conditions. However, temperature distribution shows different features at anode side with respect to cathode side. Figure 8 depicts the temperature along tube wall and along different transversal fuel cell cross sections. In the fuel channel temperature initially increases along *z* direction and reaches a maximum value of 1050 K at 60% of cell length, then temperature decreases up till the outlet section. On the other hand, in the cathode channel the outlet temperature of air is close to the inlet temperature. Air temperature increases monotonically from outlet tube section to the inlet tube section.

Average temperature is higher at the anode side since fuel mass flow rate is smaller than air mass flow rate. Lowest temperature are localized along the longitudinal axis of the air pipe, here the temperature monotonically increases due to thermal boundary layer development. The presence of the injection tube also influence the temperature distribution of the electrolyte as shown in Figure 9. Relevant gradients are localized near the inlet section and in the proximity of air tube outlet, whereas central part of the fuel cell is characterized by a uniform temperature field.

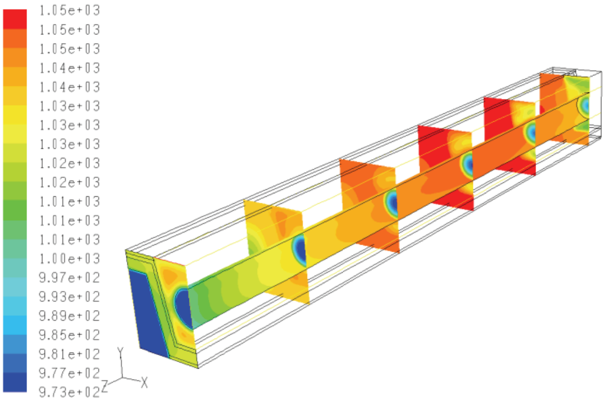

Figure 8. Temperature distribution.

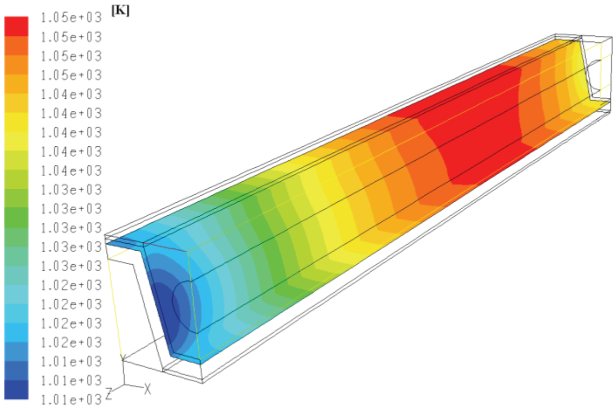

Figure 9. Electrolyte temperature.

The second fuel cell considered is localized in the top-left corner of the stack represented in Figure 1. Two sides of this cell are isolated, that is the upper interconnection plane and the left side. Vice versa the right side and the bottom plane of the cell are in contact with other cells of the stack, thus along this boundaries an heat flux is exchanged. For this cell, thermal boundary conditions are obtained with the reduced stack model and applied to the CFD single cell model. Temperature distribution of this cell is illustrated in Figure 10.

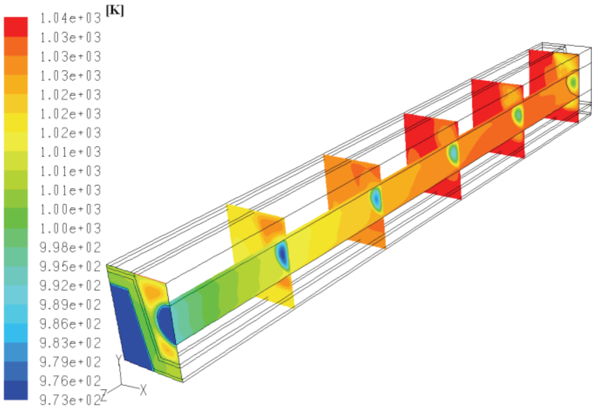

Figure 10. Temperature in the top-left corner cell.

It is possible to notice some difference if Figure 8 and Fig. 10 are compared. The asymmetric boundary conditions influence the temperature field, the heat flux coming from the right part of the stack causes an increase of air temperature flowing inside the injection tube. Consequently the air exits the pipe with a more elevate temperature. This also means that the cathodic channel temperature is higher. As a consequence the heat transported by convection is reduced as can be seen in Figure 11: the electrolyte presents a more elevated temperature close to the closed end of the cell.

4. Entropy generation analysis

The rate of entropy generation is used to choose the geometrical variables to be used in the optimization procedure and then as the thermodynamic objective function to minimized through modifications in these variables.

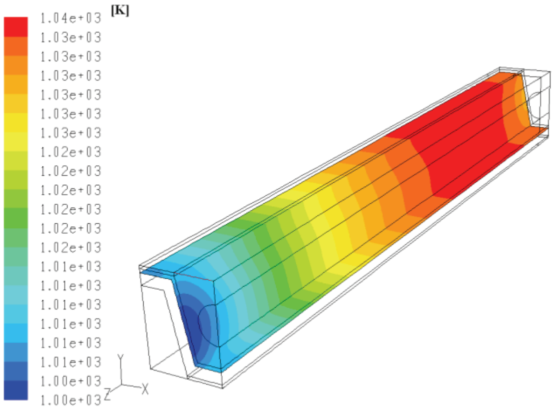

Figure 11. Electrolyte temperature of the top-left corner cell.

An expression of the rate of entropy generation in term of fluxes and the corresponding gradients of the physical quantities is used. This equation is obtained from the entropy balance written for an infinitesimal volume, developed as an equation of change (Bejan, 1982):

$$\rho \frac{Ds}{Dt} = -\nabla \cdot \vec{\sigma} + g_p \tag{4}$$

where ρ is the fluid density, s is the entropy per unit mass, $\vec{\sigma}$ is the entropy-flux vector and g_p is the rate of entropy generation per unit volume. The entropy source g_p and the entropy flux may be calculated if one makes use of the thermodynamic Gibbs relation which connects, in an isotropic multi-component fluid for instance, the rate of change of entropy s in each mass element, to the rate of change of energy u and the rates of change in composition ω_i:

$$du = Tds - pd\left(\frac{1}{\rho}\right) + \sum_i \mu_i d\omega_i \tag{5}$$

where μ_i is the chemical potential of species i.

The main aim is to relate the entropy source explicitly to the various irreversible processes that occur in a system. To this end one needs the macroscopic conservation laws of mass, momentum and energy to express the differentials in Eq. (5). Energy equation is in the form

$$\nabla \cdot \left(\vec{V}(\rho E + p)\right) = \nabla \cdot \left(k_{eff} \nabla T - \sum_\alpha h_\alpha \vec{J}_\alpha\right) + S_h \tag{6}$$

where ρ is the density of the mixture, $\vec{V}$ is the gas velocity, k_{eff} is the equivalent thermal conductivity of the solid phase and of the gas mixture, S_h is the energy source term due to electrochemical reactions and Joule heating effect. The conservation of species is

$$\nabla \cdot \left(\rho \omega_i \vec{V}\right) = -\nabla \cdot \vec{J}_i + S_i \tag{7}$$

where ω_i is the mass fraction, $\vec{J}_i$ is the diffusion flux of species i and S_i is the source term related to chemical reactions. The fluid flow equations are the continuity equation and the momentum equation (Bird et al., 2002):

$$\nabla \cdot \rho \vec{V} = 0 \tag{8}$$

$$\rho(\vec{V}\cdot\nabla)\vec{V} = -\nabla p + \mu\nabla^2\vec{V} - \frac{\mu}{K}\vec{V} \tag{9}$$

where p is the pressure, μ is the fluid viscosity. The last term of last equation appears only in the case of porous media (K is the porosity).

After some rearrangement it is possible to show that:

$$\vec{\sigma} = \frac{1}{T}\left(\vec{J_q} + \sum_{\mathrm{i}} \mu_{\mathrm{i}}\vec{J_\imath}\right) \tag{10}$$

$$g_p = \frac{1}{T}\Delta:\tau + \frac{1}{T^2}\left(-\vec{J_q}\cdot\nabla T\right) + \frac{1}{T}\left(\sum_i -\vec{J_\imath}\cdot\nabla\mu_i\right) + \frac{1}{T}\left(\sum_i -s_i\vec{J_\imath}\cdot\nabla T\right) \tag{11}$$

The first formula shows that for open systems the entropy flow consists of two parts: one is the reduced heat flow $\vec{J_q}/T$, the other is connected with the diffusion flows of matter $\vec{J_k}$. The second formula demonstrates that the entropy production contains different contributions. The first term on the right-hand side of Eq. (11) is connected to the gradients of the velocity field, giving rise to viscous flow, the second arises from heat conduction, the third from diffusion, and the fourth is due to coupling between heat and mass transfer (convective term). This means that the local rate of entropy generation is split in four main contributions, each strictly correlates to a specific physical phenomenon:

$$g_p = g_\mu + g_h + g_m + g_c \tag{12}$$

The structure of the expression for g_p is that of a bilinear form: it consists of a sum of products of two factors. One of these factors in each term is a flow quantity (heat flow, diffusion flow, momentum flows). The other factor in each term is related to a gradient of an intensive state variable (gradients of temperature, chemical potential and velocity). Further details about the capability and the limitations of this flux-force generation rate relationship can be found at (Lebon et al., 2008)

In the case of a fuel cell, an additional term must be considered in Equation (11). This term is associated with the entropy generation due to ohmic losses:

$$g_{ohm} = \frac{1}{T}\sigma\nabla\varphi\cdot\nabla\varphi \tag{13}$$

The previous term is present only in conductive regions, that is electrodes and electrolyte.

When radiation heat transfer is considered, a corresponding entropy generation term must be considered. As in this paper when only surface to surface radiation is considered, the specific entropy generation rate refers to the unit surface. Its expression is obtained considering a surface at a temperature T receiving radiation from the surrounding emitting surfaces. The infinitesimal emitting surface dA_i is at temperature T_i and the corresponding heat flux is J_{q,rad_i}:

$$g_{rad} = \int J_{q,rad_i}\left(\frac{1}{T} - \frac{1}{T_i}\right)\cdot dA_i \tag{14}$$

Local rate of entropy generation due to viscous effects in four longitudinal cross sections [(a) z=20 mm; (b) z=40 mm; (c) z=60 mm; (d) z=80 mm] is depicted in Figure 12. The largest values of g_μ are localized where there are strong velocity gradients. In particular, they take place in a small area near the walls of air-tube and cathode channel. In addition, viscous effects are also significant in the outlet tube zone, this fact is related to the presence of vortex structures which increase the viscous stresses. The largest contributions to g_μ are localize inside the air-tube and is concentrated in a layer adjacent to the wall tube. The thickness of this layer increase along the cell due to the development of velocity boundary layer.

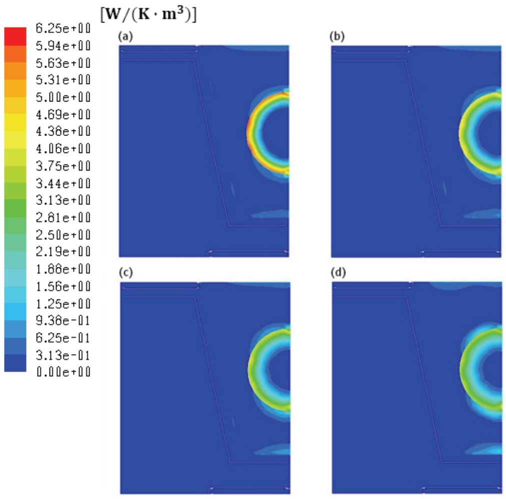

Figure 12. Viscous entropy generation.

The contribution to entropy generation due to the mass transfer is illustrated in Figure 13. The electrochemical reactions cause strong species mass fraction gradients. These gradients are the sources of entropy generation. The irreversibilities are relevant in the porous electrodes, where species motion is driven by diffusion, i.e. species concentration gradients. Large entropy production due to mass transfer is concentrated at the corners of the cell. Moreover the entropy generation distribution correctly captures where losses are predominant at the cathode side, i.e. along the upper plane of the cell.

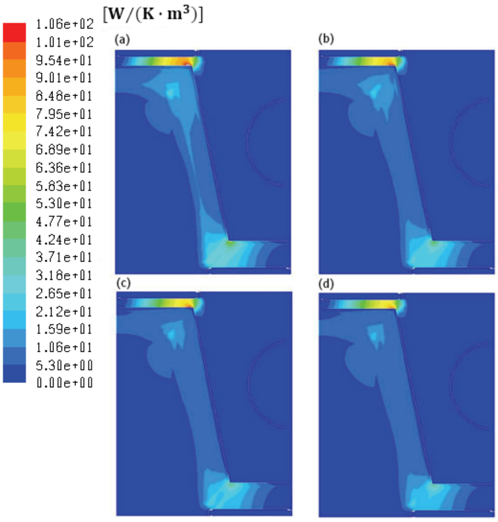

Figure 13. Entropy generation due to mass transfer on cross section planes.

The entropy generation due to heat transfer in the cell centered in the stack is shown in Figure 14. This contribution is mainly located near the tube, where strong temperature gradients are localized. In the cathode channel the temperature is lower than on fuel side, thus entropy generation is larger. Cross-section plots of heat entropy generation show that the irreversibility sources at cathode side decrease along the cell. However, the area where g_h is non-negligible increase along the cell. The same kind of irreversibility is represented in Figure 15 for the case of the fuel cell located in the external part of the stack.

Entropy generation is still confined inside the injection pipe, however irreversibility is also present along the tube mid-plane because of higher heat flux from the right. Local value of g_h are higher than in the case illustrated in Fig. 14. This source of irreversibility is negligible in the remain part of the cell because of small temperature gradients.

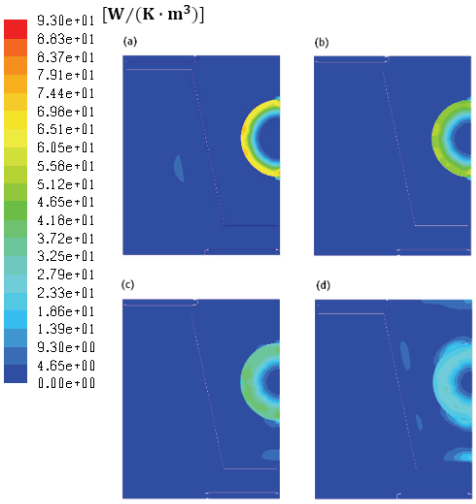

Figure 14. Entropy generation due to heat transfer.

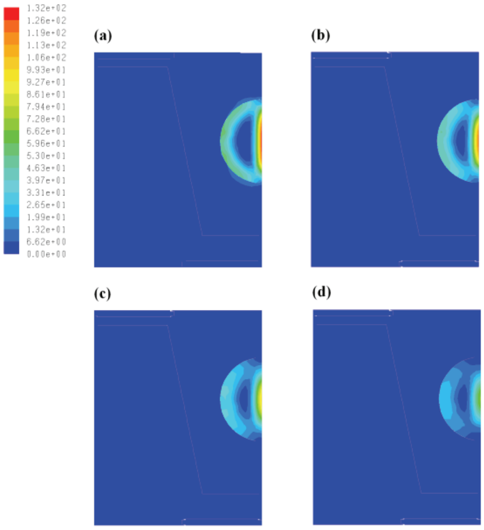

Figure 15. Entropy generation due to heat transfer in the top left cell.

5. Geometry optimization

The fuel cell optimization is performed by considering the global entropy generation rate as the objective function to minimize, namely:

$$G_p = \int \left(g_\mu + g_h + g_m + g_c + g_{ohm} \right) dV + \int g_{rad} dA \quad (15)$$

Each term of Eq. (15) is considered separately, in order to understand which are the main causes of irreversibility and thus identify a possible way to drive the optimization. The cell considered in the optimization is the one in central part of the stack.

Since we are interested in the shape optimization of the cell, it is necessary to properly parameterize the SOFC geometry in order to define the design variables free to vary. In this work we select the scaling factors along x (Xscale), y (Yscale) and z (Zscale) together with the injection tube diameter as the design parameters. The initial design of the fuel cell is shown in Figure 16a. This geometry has been obtained from a previous work, focused on the geometry improvement of the fuel cell cross section based on the analysis of the different contributions to the entropy generation (Sciacovelli and Verda, 2009). In Figure 16b it is shown a possible modified geometry which can arise from the optimization. Scaling factor along x is defined as $L_x/L_{x,0}$ while scaling factor along y is defined as $L_y/L_{y,0}$. In Figure 16b, a case where the Yscale factor is less than 1 and the Zscale factor is larger than 1 is considered.

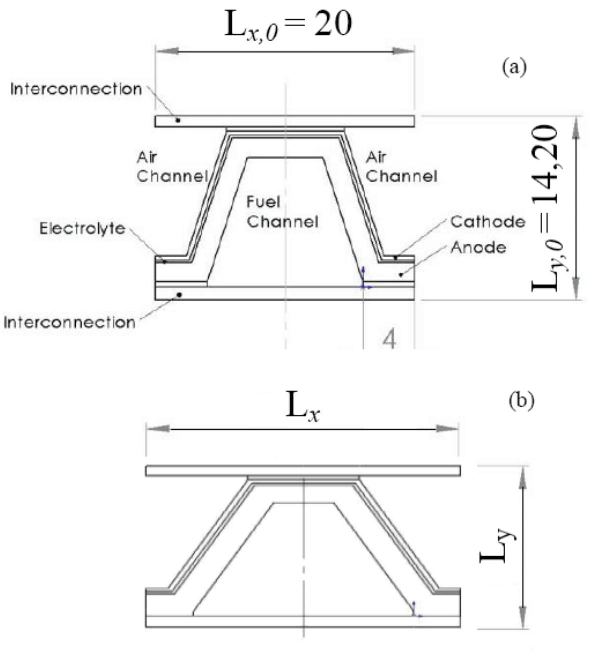

Figure 16. Entropy generation due to heat transfer.

Scaling factors have been selected in order to reduce the peak values of entropy generation occurring in the anodic channel. In particular, scaling factor along x is expected to affect the entropy generation due to heat transfer mainly, while scaling factor along y is expected to affect the entropy generation due to the coupling between heat and mass transfer. Finally the injection tube diameter is expected to affect radiation heat transfer.

In the optimization procedure the total active surface has been constrained to a fixed value. Thus, the total TPB sites for electrochemical reactions are constant for all the examined geometries. This means that the scaling factor along z is obtained from the values of the two other scaling factors together with the constraint on the active surface.

The SIMPLEX algorithm is used to perform the optimization as it is a single objective function problem (see for example Rao, 1996). The optimization process follows the following steps: the optimization algorithm generates a set of numbers, i.e. the geometrical design variables, representing the fuel cell shape. These parameters are sent to the mesh generator which creates and passes the computational grid to the CFD solver. This solver computes the conservation equations and the objective function to minimize. Finally, the numerical values of objective functions are sent back to the optimizer, which generate a new case, and so on.

In Figure 17 a bubble chart is depicted. This representation is used as the data have a third and fourth dimension that need to be shown on the same chart. In this case, the *x* and *y* scaling factor are reported along abscissa and ordinate, the diameter of the bubble indicates the *z* scaling factor, finally the color maps shows the global entropy generation in the fuel cell.

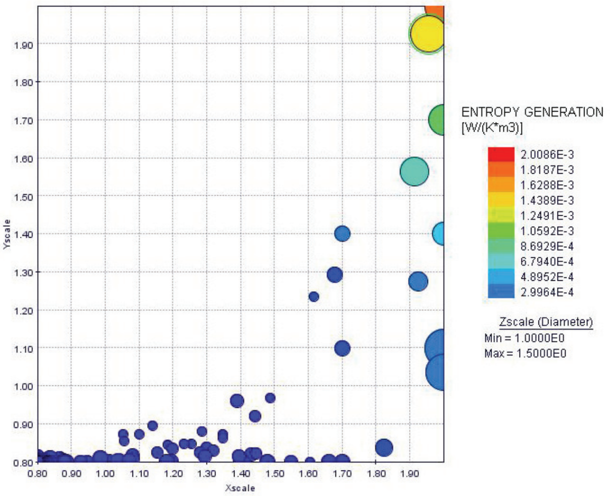

Figure 17. Bubble chart of entropy generation.

Various geometries analyzed during the optimization process are considered in Figure 18. The figure shows that a reduction in the entropy generation leads to an increase in the electric power produced per unit active area (i.e. an increase in the current density, as the operating voltage is fixed). This is particularly important as power density is one of the main parameters that can reduce the fuel cell investment costs.

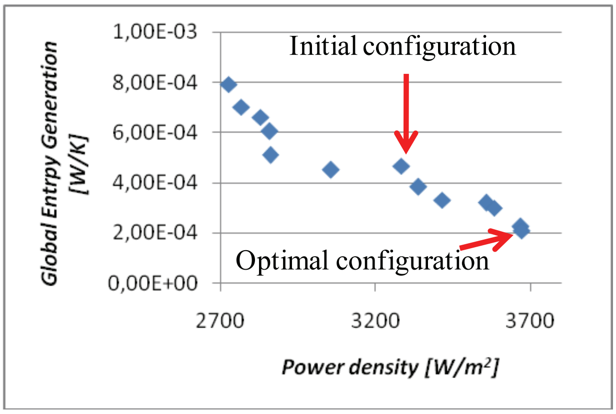

Figure 18. Entropy generation vs. Power density.

The optimal configuration is obtained for the X scale = 1.4 and the Y scale = 0.8, which means that the optimal length in the *y* direction is smaller than in the initial design, while the length in the *x* scale is larger. This shape allows one to reduce the fluid flow_resistances towards the active surface, in correspondence to the upper edge, where the entropy generation due to mass transfer presents high picks. Concerning the injection tube diameter, the optimal value is 2.5 mm which was established as the minimum value. Figure 19 shows the effect of the injection tube diameter on the power density. It is shown that power density increases with reducing diameter, but below a diameter of 3.5 mm this effect is small and below 2.5 mm, which is not represented in the Figure, viscous effects increases considerably, which causes a reduction in power density

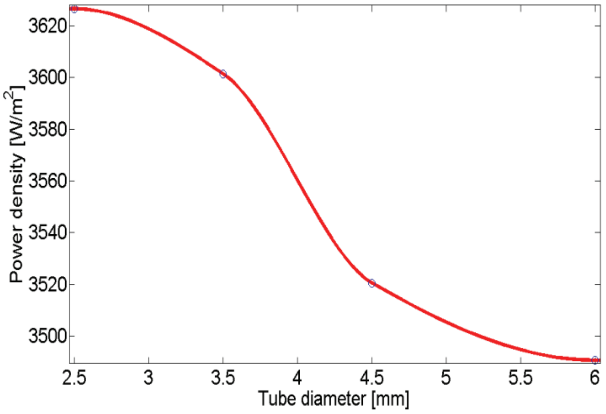

Figure 19. Effect of tube diameter on power density.

6. Conclusions

In this paper, the optimization of the geometry of a tubular solid oxide fuel cell is conducted using the minimum entropy generation as the objective function.

The separate contributions to the entropy generations are also calculated: heat transfer, viscous flow, coupling between heat and mass transfer, diffusive term, and current transfer. In addition, as radiation heat transfer has been considered in the model, the impact of this term on the entropy generation has been evaluated. In order to take into account realistic operating conditions, a network stack model has been adopted to solve the thermal problem.

The choice of the design parameters is performed on the basis of values assumed by the various contributions to the total entropy generation. In particular, the injection tube diameter is selected as it affects the entropy generation due to radiation heat transfer. The scaling actors are considered as they affect the contributions to conduction and to convection heat transfer.

With respect to the initial design, the entropy generation in the optimized geometry is reduced of about 50%, while the power density is increased of about 10%. Another benefit that can be achieved in the optimization consists in the fuel cell volume. As this may be an issue in the design process, it is worth to consider a multi-objective optimization assuming entropy generation and volume as the two objective functions.

Nomenclature

$I(\vec{r},\vec{s})$	Radiation Intensity (W m^{-2} Sr^{-1})
$\vec{J}_i$	Diffusive flux of species *i* (kg m^{-2} s^{-1})
$\vec{J}_q$	Heat flux (W m^{-2})
K	Permeability (m^{2})
a	surface absorption coefficient
k	Thermal conductivity (W m^{-1} K^{-1})
p	Pressure (Pa)
R	Universal gas constant (J mol^{-1} K^{-1})
S_i	Species source term (kg m^{-3} s^{-1})
g_p	Total entropy generation per unit volume (W m^{-3} K^{-1})
g_μ	Fluid friction entropy generation per unit volume (W m^{-3} K^{-1})
g_h	Heat transfer entropy generation per unit volume (W m^{-3} K^{-1})
g_m	Mass transfer entropy generation per unit

	volume (W m^{-3} K^{-1})
g_c	Heat – mass transfer entropy generation per unit volume (W m^{-3} K^{-1})
g_p	Total entropy generation per unit volume (W m^{-3} K^{-1})
g_{rad}	Radiative heat transfer entropy generation per unit surface (W m^{-2} K^{-1})
T	Temperature (K)
$\vec{V}$	Velocity vector (m s^{-1})

Greek

$\Phi(\vec{s},\vec{s}')$	Phase function (W m^{-2} Sr^{-1})
φ	Potential (V)
β	Transfer coefficient
Δ	Strain tensor (s^{-1})
ε	porosity
μ	Viscosity (m s^{-2})
μ_i	Chemical potential of species *i*
ρ	Density (kg m^{-3})
σ	Electric conductivity (Ω^{-1} m^{-1})
σ_b	Stefan-Boltzmann constant (W m^{-2} K^{-1})
σ_s	Scattering coefficient
$\vec{\sigma}$	Entropy flux
ω_i	Mass fraction of species *i*

References:

A. Bejan, Entropy Generation through Heat and Fluid Flow, Wiley, New York, 1982.

Bird R. B., Stewart W. E., Lightfoot E. N., *Transport Phenomena*, 2nd ed. New York: John Wiley & Sons, 2002.

Calì M., Santarelli M.G.L., Leone P. (2006). Computer experimental analysis of the CHP performance of a 100kWe SOFC Field Unit by a factorial design. Journal of Power Sources. 156; 400–413.

Chui E. H. and Raithby G. D., "Computation of Radiant Heat Transfer on a Non-Orthogonal Mesh Using the Finite-Volume Method," *Numerical Heat Transfer, Part B*, vol. 23, pp. 269-288, 1993.

Ciano C., Calì M., Verda V. (2009). "Analysis of Entropy Generation for the Performance Improvement of a Tubular Solid Oxide Fuel Cell Stack". Int. J. of Thermodynamics Vol. 12 (No. 1), pp. 1-8.

Damm D., Fedorov G. (2005). "Radiation heat transfer in SOFC materials and components" Journal of Power Sources 143, 158–165.

Fischer K, Seume J (2006) Location and magnitude of heat sources in solid oxide fuel cells. In: Proceedings of FUELCELL2006.

Gubner A., Froning D., Haart B., Stolen D., (2003). Complete modeling of kW-range SOFC stacks, ECS Proc. 17, pp. 1436-1441.

Haynes C, Wepfer WJ (2001) Characterizing heat transfer within a commercial-grade tubular solid oxide fuel cell for enhanced thermal management. Int J of Hydrogen Energy 26:369-379.

Hwang J.J., Chen C.K., Lai D.Y. (2005). Computational analysis of species transport and electrochemical characteristics of a MOLB-type SOFC. Journal of Power Sources 140; 235–242.

Ki J., Kim D. (2010). "Computational model to predict thermal dynamics of planar solid oxide fuel cell stack during start-up process". Journal of Power Sources 195; 3186–3200.

Krishna R., Wesselingh J. A. (1997). The Maxwell-Stefan approach to mass transfer. Chemical Engineering Science, Vol. 52, No. 6, pp. 861-911.

Larminie J., Dicks A. (1999). Fuel cell systems explained. Wiley.

Lebon G., Jou D., Casas-Vàzques (2008). Understanding Non-equilibrium Thermodynamics: Foundations, Applications, Frontiers. Springer-Verlag, Berlin, 2008

Lee S.F., Hong C.W. (2010). "Multi-scale design simulation of a novel intermediate temperature micro solid oxide fuel cell stack system". International Journal of Hydrogen Energy 35; 1330-1338.

Li PW, Suzuki K (2004) Numerical modeling and performance study of a tubular SOFC. Journal of the Electrochemical Society 151:A548-A557.

Modest M.F., *Radiative Heat Transfer*, 2nd ed. New York: Academic Press, 2003.

National Energy Technology Laboratory, U.S. Department of Energy (2004). Fuel Cell Handbook. <http://www.netl.doe.gov>

Ota T, Koyama M, Wen C, Yamada K, Takahashi H (2003) Object-based modeling of SOFC system: dynamic behavior of micro-tube SOFC. Journal of Power Sources 118:430-439.

Patankar S.V. (1980). Numerical heat transfer and fluid flow. Hemisphere. Washington DC

Pramuanjaroenkij A., Xiang Yang Zhou and Kakaç S., (2007) "A review of numerical modeling of solid oxide fuel cells," *International Journal of Hydrogen Energy*, vol. 32, no. 7, pp. 761-786.

Rao, S.S. (1996). Engineering Optimization: Theory and Practice, 3rd Edition. John Wiley and Sons.

Sciacovelli A., Verda V. (2008). Entropy generation minimization in a tubular solid oxide fuel cell. ASME paper IMECE2008-68910. Proceedings of IMECE 2008, Boston, Massachusetts, October 31 - November 6.

Sciacovelli A., Verda V. (2009). "Entropy Generation Analysis in a Monolithic-Type Solid Oxide Fuel Cell (SOFC)". Energy, 34, pp. 850-865.

Verda V., Calì M. (2007). "Performance Analysis of Solid Oxide Fuel Cell Stack. Part 1: Model description and validation", ASME Paper, *IMECE 2007-43627*, Seattle, WA, November 11 - 15.

Verda V, De Benedictis F, Disegna G, Orsello G. Operation of the Siemens SOFC Generators CHP100 and SFC5 in a Mechanical Factory. In: Proceedings of the ASME Conference on Engineering Systems Design and Analysis ESDA 2008. Haifa, Israel; July 7–9, 2008.

Yang Y., Wang G., Zhang H., Xia W (2008). Comparison of heat and mass transfer between planar and MOLB-type SOFCs. Journal of Power Sources 177; 426–433.